

A Study on the Largest Hydraulic Fracturing Induced Earthquake in Canada: Numerical Modeling and Triggering Mechanism

Bei Wang^{1,2}, Alessandro Verdecchia³, Honn Kao^{*1,2}, Rebecca M. Harrington⁴, Yajing Liu³, and Hongyu Yu²

ABSTRACT

The M_w 4.6 earthquake that occurred on 17 August 2015 northwest of Fort St. John, British Columbia, is considered the largest hydraulic-fracturing-induced event in Canada, based on its spatiotemporal relationship with respect to nearby injection operations. There is a ~ 5 day delay of this M_w 4.6 mainshock from the onset of fluid injection at the closest well pad (W1). In contrast, other two nearby injection wells (W2 and W3) have almost instantaneous seismic responses. In this study, we first take a forward numerical approach to investigate the causative mechanisms for the M_w 4.6 event. Specifically, three finite-element 3D poroelastic models of various permeability structures and presence or absence of hydraulic conduits are constructed, to calculate the coupled evolution of elastic stress and pore pressure caused by multistage fluid injections. Our simulation results suggest that pore pressure increase associated with the migration of injected fluid is required to accumulate sufficient stress perturbations to trigger this M_w 4.6 earthquake. In contrast, the elastic stress perturbation caused by rock matrix deformation alone is not the main cause. Furthermore, injection and seismicity at W1 may have altered the local stress field and brought local faults closer to failure at sites W2 and W3. This process could probably shorten the seismic response time and, thus, explain the observed simultaneous appearance of injection and induced seismicity at W2 and W3.

KEY POINTS

- Pore pressure change caused by fluid migration most likely triggered the largest induced earthquake in Canada.
- Injection and other factors may alter local stress field that, in turn, affect the seismic response time.
- Avoiding preexisting faults and high-permeable structures help mitigate seismic hazard from induced events.

Supplemental Material

INTRODUCTION

For the past decade, the sharp increase in seismicity in the central United States has been attributed to the wastewater injection through disposal wells, and the majority of events occur deeper than the target injection layers within the basement rocks (e.g., Ellsworth, 2013; Kim, 2013; Keranen *et al.*, 2014; Weingarten *et al.*, 2015). In contrast, studies suggest that hydraulic fracturing (HF) could be responsible for the majority of induced earthquakes in the Western Canada Sedimentary Basin (WCSB) (Fig. 1) (e.g., B.C. Oil and Gas Commission, 2012; Atkinson *et al.*, 2016; Mahani *et al.*, 2017; Schultz *et al.*, 2018; Yu *et al.*, 2019; Roth *et al.*, 2020). On 17 August 2015, an

M_w 4.6 earthquake occurred within the southern Montney Play northwest of Fort St. John, British Columbia. The epicenter of this earthquake was located within 500 m of an actively stimulated well and less than 7 km of two nearby wells (Fig. 1). This event has been recognized as the largest HF-induced event in Canada.

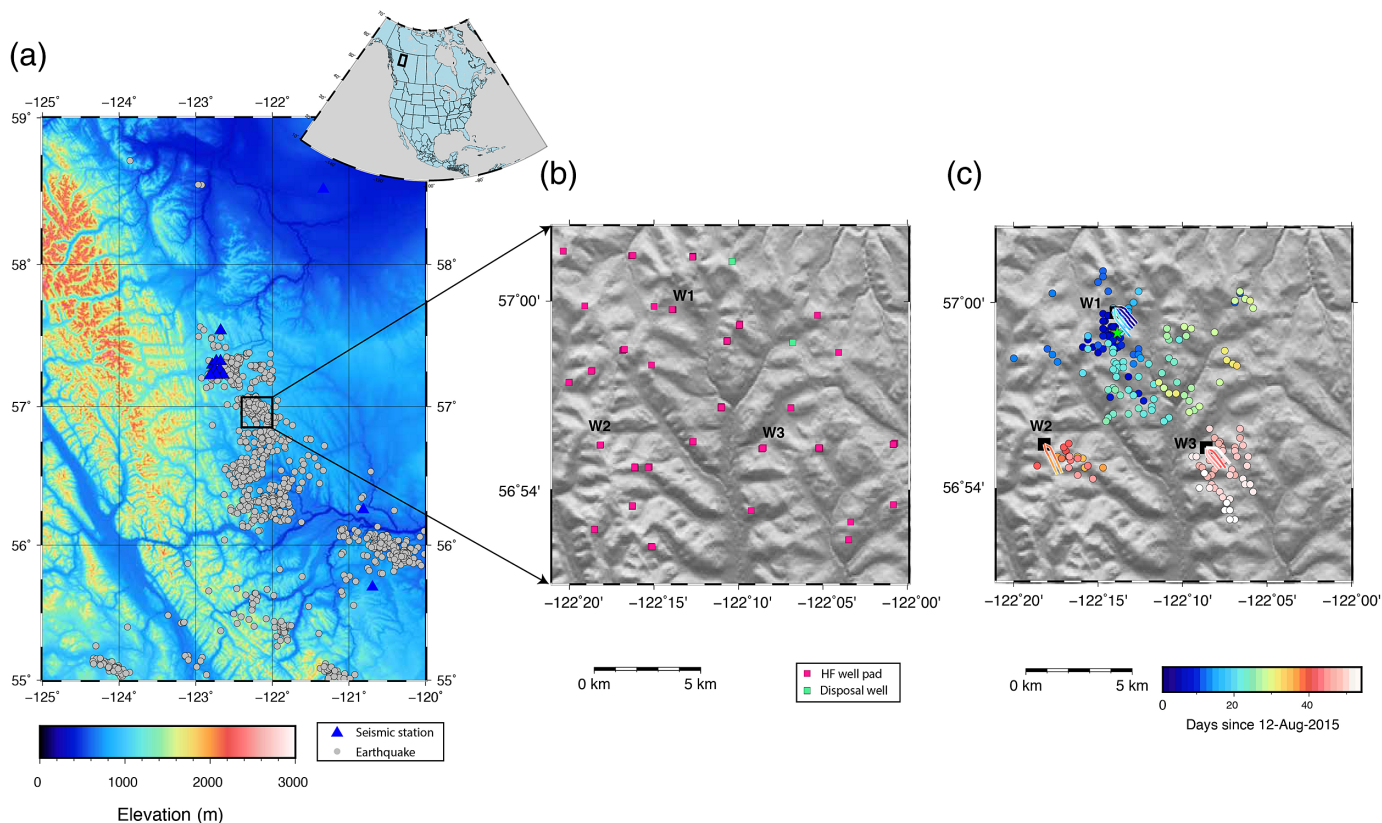
A previous study (Wang *et al.*, 2020) investigated the source characteristics of this M_w 4.6 sequence and found: (1) a clear spatiotemporal relationship between the local HF operations and the observed earthquake sequence (Fig. 1, W1, W2, and W3 are the only active wells in the study area during the time of this event), (2) static stress drop values of the induced earthquakes falling within the typical range of tectonic events, and (3) significant variation in the seismic response times at nearby

1. School of Earth and Ocean Sciences, University of Victoria, Victoria, Canada; 2. Geological Survey of Canada, Pacific Geoscience Centre, Sidney, British Columbia, Canada; 3. Department of Earth and Planetary Sciences, McGill University, Montreal, Quebec, Canada; 4. Ruhr-University Bochum, Institute of Geology, Mineralogy, and Geophysics, Bochum, Germany

*Corresponding author: honn.kao@canada.ca

Cite this article as Wang, B., A. Verdecchia, H. Kao, R. M. Harrington, Y. Liu, and H. Yu (2021). A Study on the Largest Hydraulic Fracturing Induced Earthquake in Canada: Numerical Modeling and Triggering Mechanism, *Bull. Seismol. Soc. Am.* **XX**, 1–13, doi: 10.1785/0120200251

© Seismological Society of America



wells, even though the injection sites are located less than 10 km apart. For example, the first recorded event occurred five days after the onset of injection, at the closest well pad W1, whereas at two nearby wells—W2 and W3—earthquakes occurred nearly simultaneously (within 1 day) after the operation started. The locations of the three wells are shown in Figure 1c. Based on the observations, Wang et al. (2020) infer that this M_w 4.6 earthquake occurred on a preexisting fault, with a significant amount of preloaded tectonic strain.

However, there are still remaining questions about the seismogenic behaviors of the M_w 4.6 earthquake sequence. For example, what is the most plausible triggering mechanism for the mainshock? Why is the seismic response at the two nearby HF wells (W2 and W3) much faster compared to the ~ 5 day delay at W1? Although, multiple studies have proposed several potential triggering mechanisms, to explain induced seismicity, for example, the poroelastic effects transmitted by the rock matrix (e.g., Deng et al., 2016; Yu et al., 2019), the pore pressure diffusion on a larger scale (e.g., Healy et al., 1968; Hsieh and Bredehoeft, 1981; Garagash and Germanovich, 2012; Bao and Eaton, 2016; Azad et al., 2017; Galis et al., 2017; Schultz et al., 2018; Yu et al., 2019; Maurer et al., 2020; Yu et al., 2020), and stress transfer to distant faults through aseismic slip (e.g., Guglielmi et al., 2015; Eyre et al., 2019; Bhattacharya and Viesca, 2019), a comprehensive study is necessary to investigate the most plausible triggering mechanism for this specific case. The objective of this

Figure 1. (a) Seismicity in northeastern British Columbia during 2011–2020, reported by Natural Resources Canada. The black rectangle marks the study area. The inset shows the location of northeastern British Columbia in North America. (b) Hydraulic fracturing (HF) pads and disposal wells in the study area. (c) The spatiotemporal distribution of the induced earthquakes from Wang et al. (2020), the colors of the wells and earthquakes correspond to occurrence time since 12 August 2015, and the green star denotes the M_w 4.6 mainshock. The color version of this figure is available only in the electronic edition.

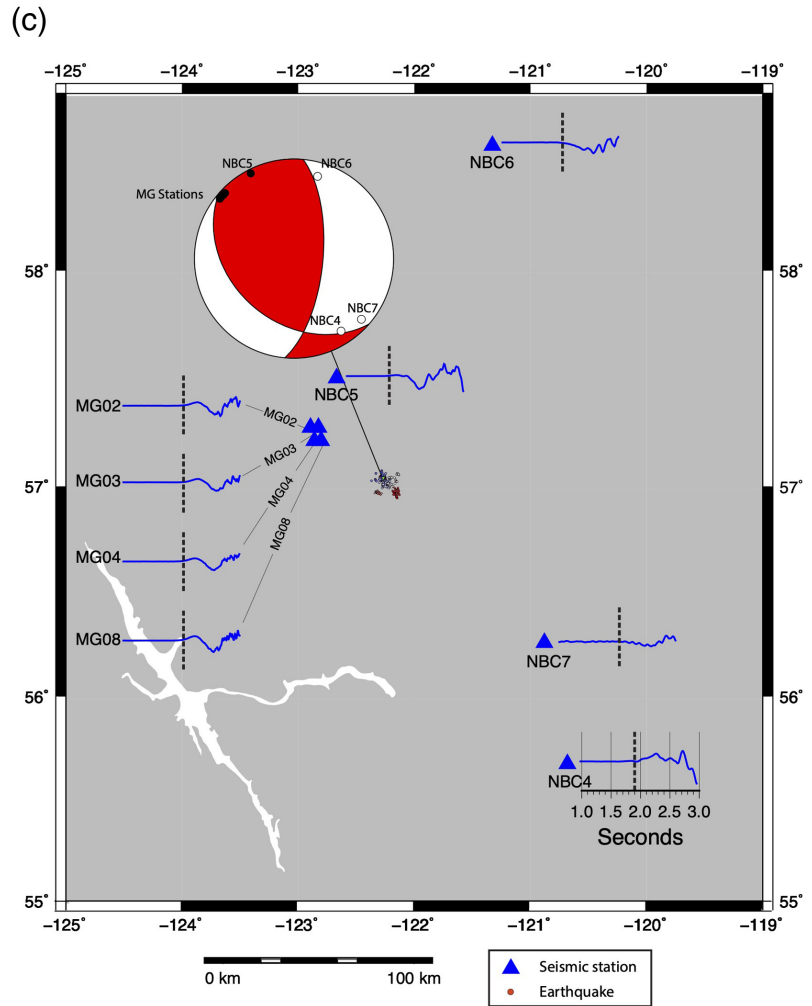
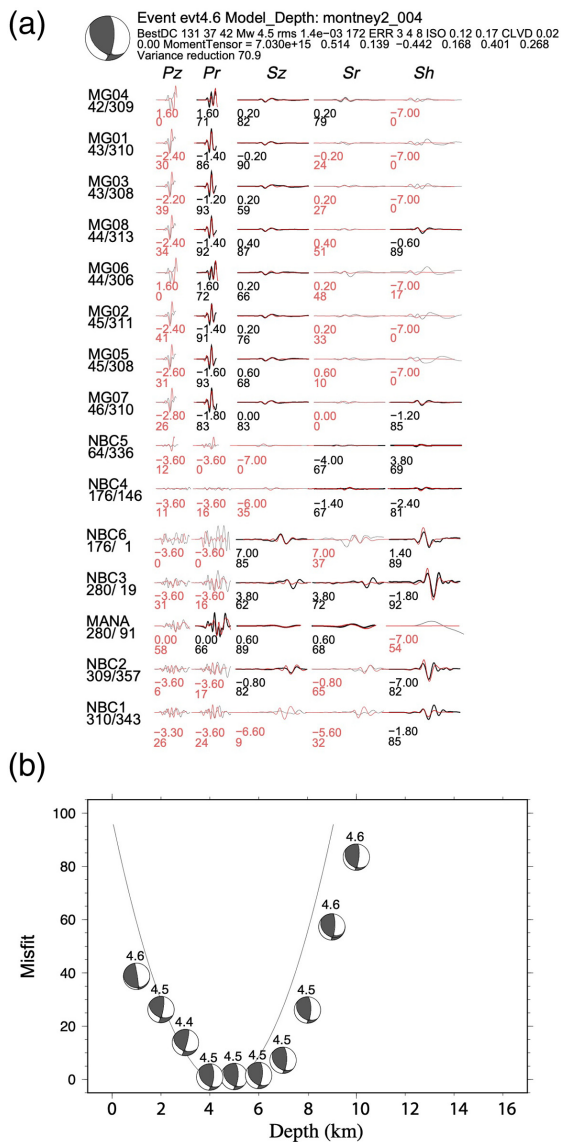
study is to investigate the various aspects of seismogenesis of the M_w 4.6 earthquake and the different response times of the three HF sites in close proximity. To do so, we use 3D poroelastic models with detailed numerical simulations of the geo-mechanical evolution caused by fluid injection.

METHOD

In this study, we use the Coulomb failure criterion to study the relationship between HF fluid injection and activation of the fault plane that hosted the M_w 4.6 event (e.g., Harris, 1998; Steacy et al., 2005). The change of Coulomb stress (ΔCFS) on a fault plane can be defined as follows:

$$\Delta CFS = \Delta\tau + \mu(\Delta\sigma + \Delta p), \quad (1)$$

in which $\Delta\tau$ is the shear stress change, and $\Delta\sigma$ is the normal stress change resolved onto a fault plane and is considered



positive in tension, μ is the friction coefficient, and Δp is the pore pressure change. Positive ΔCFS will favor slip and vice versa (e.g., Harris, 1998; Stein, 1999).

We first calculate the focal depth and focal mechanisms for the target M_w 4.6 earthquake, with the generalized cut-and-paste (gCAP) method (Zhu and Helmberger, 1996), as the amplitude of the normal and shear stress is directly related to the location and orientation of the fault (e.g., Lin and Stein, 2004). We then use the COMSOL Multiphysics software, to simulate the coupled evolution of elastic stress and pore pressure caused by HF fluid injection, and then calculate the ΔCFS resolved on the M_w 4.6 receiver fault. Finally, we use the same approach to calculate the ΔCFS resolved on optimally oriented faults and investigate the different seismic response times at the two nearby HF injection sites (W2 and W3).

Focal mechanism determination

We use the gCAP method, to determine the moment-tensor solution for the M_w 4.6 earthquake by inverting the body

Figure 2. Focal mechanism solutions for the M_w 4.6 earthquake. (a) Synthetic and observed seismograms are plotted as red and black lines, respectively. Lines with black numbers below are the matches used in the inversion, whereas, lines with red numbers below are discarded pairs. (b) Misfit error of moment tensor inversion versus depth by generalized cut-and-paste (gCAP) method. (c) The confidence check by P -wave polarities. Black circles indicate stations with positive polarity (upward), and white circles indicate negative polarity (downward). The color version of this figure is available only in the electronic edition.

and surface waveforms recorded at local distances (Fig. 2), together with the P -wave first-motion method as a consistency check.

The gCAP method estimates the full moment tensor through a grid search over the complete model space of the strike, dip, and rake angles of a fault, then decomposes the moment tensor into three source terms: isotropic, double-couple, and compensated linear vector dipole. We first compute the Green's functions for a wide range of distances

(50–350 km), with the frequency–wavenumber integration approach (Aki and Richards, 2002; Zhu and Rivera, 2002). We adopt the same regional 1D velocity model used in the routine moment tensor inversion, for significant earthquakes in western Canada (Kao *et al.*, 2012; Fig. S1, available in the supplemental material to this article). We then filter the original seismograms, using a band-pass filter in the frequency bands 0.05–0.3 Hz and 0.02–0.1 Hz for the *P* and *S* waves, respectively, and cut the three component records into five phase windows, including the radial and vertical components of the *P* phase and the transverse, radial, and vertical of the *S* phase (e.g., Yu, Liu, *et al.*, 2016; Yu, Zhao, *et al.*, 2016). We apply the same band-pass filter to synthetic seismograms as well. Finally, we calculate the misfit between the synthetic and observed waveforms to find the final solution. We allow a time shift (up to 7 s) between the synthetic and observed waveforms for each phase, to account for any mislocation of the epicenter. Figure 2a shows the example of the synthetic and observed seismograms match at 4 km depth, in which the numbers in the first row below the seismogram matches indicate the time shift, whereas the numbers in the second row indicate the variance reduction of each match.

We repeat the moment tensor inversion for each depth in the range of 1–10 km, and the solution with the lowest overall misfit is found at a depth of 4 km (Fig. 2b), which is also comparable to the depth solution of 3.5 km from Wang *et al.* (2020). Our solution shows a slightly oblique thrust mechanism with northwest–southeast nodal planes (nodal plane 1: strike 131°, dip 37°, and rake 42°; nodal plane 2: strike 5°, dip 66°, and rake 119°). The consistency check, using the available *P*-wave first motions, has been shown in Figure 2c, exhibiting consistent polarities with the gCAP focal mechanism solution, with the exception of station NBC4, which is located close to one of the nodal planes.

Poroelastic model

Analytic and numerical models have been widely used to study stress changes caused by injection and their relation to seismicity (e.g., Segall and Lu, 2015; Bao and Eaton, 2016; Deng *et al.*, 2016; Goebel *et al.*, 2017; Yu *et al.*, 2019). Both pore fluid pressure increase and poroelastic stress perturbations have been proposed as potential mechanisms. Here, we use the COMSOL Multiphysics software (version 5.3a) to model the distribution and evolution of pore pressure and poroelastic stress surrounding the injection wells W1–W3 (Fig. 1).

We use the solid mechanism module and Darcy’s fluid flow module, to simulate the poroelastic coupling process. By assuming an isotropic and homogeneous medium, the pore pressure can be obtained by solving the coupled diffusion equation (similar equivalent forms of the equations can be

found, e.g., Wang and Kumpel, 2003; Shapiro and Dinske, 2009),

$$\rho S \frac{\partial p}{\partial t} - \nabla \cdot \left(\rho \frac{\kappa}{\mu_d} \nabla p \right) = Q_m(x, t) - \rho \alpha \frac{\partial \varepsilon_{\text{vol}}}{\partial t}, \quad (2)$$

$$S = \chi_f \epsilon + \chi_p (1 - \epsilon), \quad (3)$$

$$q = -\frac{\kappa}{\mu_d} \nabla p, \quad (4)$$

in which $\nabla \cdot$ is a divergence operator, S is the linearized storage parameter, p is the fluid’s pressure in the pore space, ε_{vol} is the volumetric strain of the porous matrix, κ is the permeability of the block, Q_m is the volumetric flow rate for a fluid source, α is the Biot-Willis coefficient, ρ is the pore fluid density, μ_d is its dynamic viscosity, χ_f is the compressibility of the fluid, χ_p is the compressibility of the rock, ϵ is porosity, and q is the velocity variable, which gives a volume flow rate per unit area of the porous material. COMSOL uses S as the default parameter in equation (2), whereas some studies use the Biot modulus M^{-1} instead of S , which can be calculated from the Young’s modulus (G) and Poisson’s ratio (ν) (e.g., Rice and Cleary, 1976; Detournay and Cheng, 1993; Leake and Hsieh, 1995). The governing equations for the poroelastic model are listed subsequently:

$$-\nabla \cdot \boldsymbol{\sigma} = \mathbf{F}_v, \quad (5)$$

$$\sigma_{ij} = \frac{2G\nu}{(1-2\nu)} \varepsilon_{kk} \delta_{ij} + 2G\varepsilon_{ij} - \alpha p \delta_{ij}, \quad (6)$$

$$\varepsilon_{ij} = \frac{1}{2} ((\nabla \mathbf{u})^T + \nabla \mathbf{u}), \quad (7)$$

in which $\boldsymbol{\sigma}$ is the stress tensor, \mathbf{F}_v is the volume force vector, δ_{ij} is the Kronecker delta (equal to 1 when $i = j$, and to 0 when $i \neq j$), and \mathbf{u} is the deformation vector. When gravity is the only driving force, F_v is $(\rho\theta + \rho_b)g$, in which g is the acceleration of gravity, θ is the porosity, and ρ_b is the bulk density.

Δ CFS calculation

The Δ CFS has been widely used to interpret the causality of earthquake triggering, as it provides a quantitative estimation for the evolution of the stress field and the likelihood of future failure (e.g., Harris, 1998; Stein, 1999). With the stress tensor and pore pressure change calculated by COMSOL, we can get $\Delta\tau$ and $\Delta\sigma$ by projecting the stress tensor (σ_{ij}) along the slip and normal directions of a fault,

respectively. After substituting them into equation (1), we get the following equation to calculate the ΔCFS resolved on the fault plane (e.g., Xu *et al.*, 2010):

$$\begin{aligned} \Delta\text{CFS} = & \sin\lambda \left[-\frac{1}{2}\sin^2\phi \sin(2\tilde{\delta})\sigma_{11} + \frac{1}{2}\sin(2\phi) \sin(2\tilde{\delta})\sigma_{12} \right. \\ & + \sin\phi \cos(2\tilde{\delta})\sigma_{13} - \frac{1}{2}\cos^2\phi \sin(2\tilde{\delta})\sigma_{22} \\ & \left. - \cos\phi \sin(2\tilde{\delta})\sigma_{23} + \frac{1}{2}\sin(2\tilde{\delta})\sigma_{33} \right] \\ & + \cos\lambda \left[-\frac{1}{2}\sin(2\phi) \sin\tilde{\delta}\sigma_{11} + \cos(2\phi) \sin\tilde{\delta}\sigma_{12} \right. \\ & \left. + \cos\phi \cos\tilde{\delta}\sigma_{13} + \frac{1}{2}\sin(2\phi) \sin\tilde{\delta}\sigma_{22} + \sin\phi \cos\tilde{\delta}\sigma_{23} \right] \\ & + \mu[\sin^2\phi \sin^2\tilde{\delta}\sigma_{11} - \sin(2\phi) \sin^2\tilde{\delta}\sigma_{12} \\ & - \sin\phi \sin(2\tilde{\delta})\sigma_{13} + \cos^2\phi \sin^2\tilde{\delta}\sigma_{22} \\ & + \cos\phi \sin(2\tilde{\delta})\sigma_{23} + \cos^2\phi \sigma_{33} + \Delta P], \end{aligned} \quad (8)$$

in which μ is the friction coefficient (set here as 0.6), ϕ , $\tilde{\delta}$, and λ are the strike, dip, and rake of the receiver fault, respectively, σ_{ij} is the stress tensor, in which $i, j = 1, 2, 3$ are the 3D components in the Cartesian coordinate system, and ΔP is the pore pressure change. It is worth noting that, because the stress tensor and pore pressure are both time dependent, the ΔCFS is a property that also evolves with time.

NUMERICAL SIMULATION AND RESULTS

Poroelastic models for the M_w 4.6 mainshock

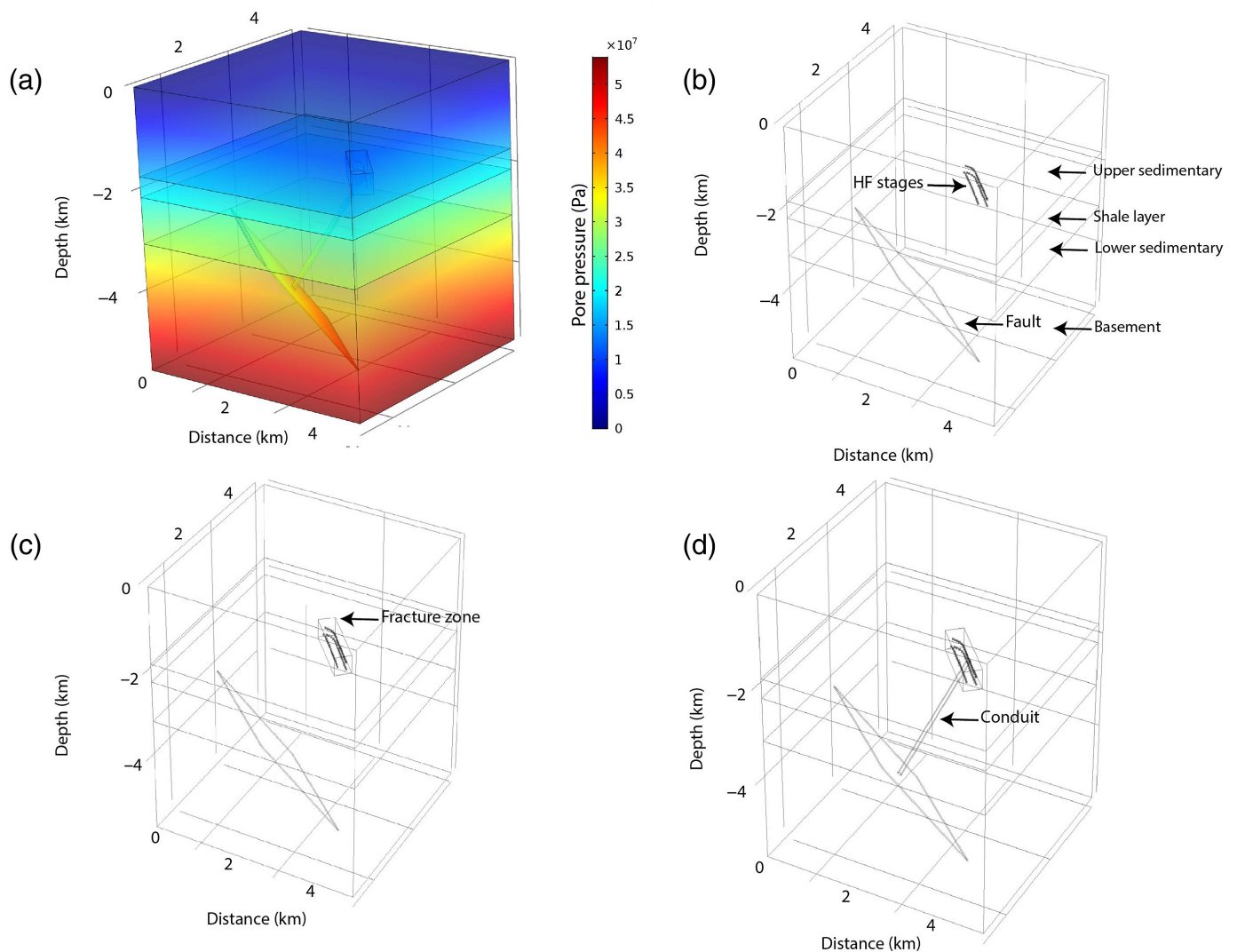
To investigate the most plausible triggering mechanism for the M_w 4.6 earthquake, we build 3D models of 5 km dimensions in all coordinate directions. We divide each model into four layers, as shown in Figure 3a, representing the upper sedimentary layer, the shale layer where the HF occurs, the lower sedimentary layer, and the crystalline basement, with depth ranges representative of the stratigraphy of our study area (e.g., Davies *et al.*, 1997). We use published data to set the solid and hydrogeological properties of each layer (Clauser, 1992; Neuzil, 1994; Rokosh *et al.*, 2008, 2010; Laske *et al.*, 2013; Dong *et al.*, 2017; Vishkai *et al.*, 2017; Cui and Nassichuk, 2018), and major properties used in the model are listed in Table S1. We also assume that the fluid properties do not change with depth or time (see Table S1). Based on the corner frequency (f_c) of ~ 3.2 Hz, derived by Wang *et al.* (2020), for the M_w 4.6 mainshock and the assumption of a circular rupture, we estimate the radius of its rupture to be 400 m (Madariaga, 1977). Consequently, we set a 3 km \times 3 km fault patch, to adequately encompass the entire circular rupture. Previous studies suggest that the hydrological characteristics along the fault surface could be very different from the surrounding rocks due to the fault's damage zone (e.g., Yehya *et al.*, 2018), so we assume that the permeability along the fault is one order of magnitude larger than the confining layers (Table S1).

With the basic model setup, we design three scenarios to investigate the influence of different hydrogeological structures on the stress field change, due to multistage injection. In model 1 (Fig. 3b), we only simulate the fluid injection for each stage, without considering the effect from any potential fractures or conduits outside of the fault surface. In model 2 (Fig. 3c), besides the fluid injection points, we assume that the HF operations have created a fracture zone surrounding the horizontal wells, leading to an increased permeability compared to the unfractured shale formation. In model 3 (Fig. 3d), we add a conduit to connect the fracture zone and the preexisting fault, in which the conduit has a permeability two orders of magnitude larger than the surrounding formations (5×10^{-12} m²), similar to the studies of Deng *et al.* (2016) and Peña Castro *et al.* (2020). The permeability of the conduit falls at the high end of observed values for fault's damage zones (e.g., Cappa, 2009; Farrell *et al.*, 2014).

Within each model, the fluid-solid boundary and initial conditions are configured as follows. We set the so-called roller condition for the side solid boundaries, that is, no perpendicular movement for the solid material on the boundary. The bottom and top solid boundaries are set as fixed and free surfaces, respectively. There is no fluid flow across all boundaries. At the top, we add the standard atmospheric pressure, and set the pore pressure as 0. We include gravity as the driving force and assume that the original fluid condition is in hydrostatic equilibrium. For setting the initial condition, we add a stationary model in which we set the initial displacement u and initial pore pressure p to be 0 within the medium, and, solve the changes in stress field and pressure, as a result of the sole gravity loading without time-dependent variables (the hydrostatic condition is shown in Fig. 3a). We then add the time-dependent model with the poroelasticity multiphysics module in COMSOL, which uses the elastic stress and pore pressure solutions from the stationary model as the initial condition.

Next, we simulate the multistage fluid injection process by assuming that fluid is injected at a single point of each stage, and the consecutive stages migrate along the horizontal well bore. However, due to the lack of precise timing of each HF stage, we arbitrarily assume that the HF operations start at eight o'clock local time each morning, and individual stages are finished without overlapping in time. The injection rate for each stage of the three wells is shown in Figures 4, 5 and Figure S2.

Figure 4a,b shows the evolutions of ΔCFS and pore pressure, respectively, on the mainshock fault surface for the three models (Fig. 4c,d is the enlarged version). The results indicate that the ΔCFS calculated on the receiver fault in both models 1 and 2 is small and negative, and would discourage slip on the fault. The small ΔCFS (albeit being negative) can be attributed to two factors: (1) a relatively small amount of fluids injected into the shale formation causing very limited solid deformation, and (2) the low permeability of the shale prevents the



fluid from reaching the preexisting fault in a short-time period, leading to a small change in pore pressure. In contrast, the ΔCFS for model 3 has a much higher and positive value, ~ 0.56 MPa, which works to encourage fault slip.

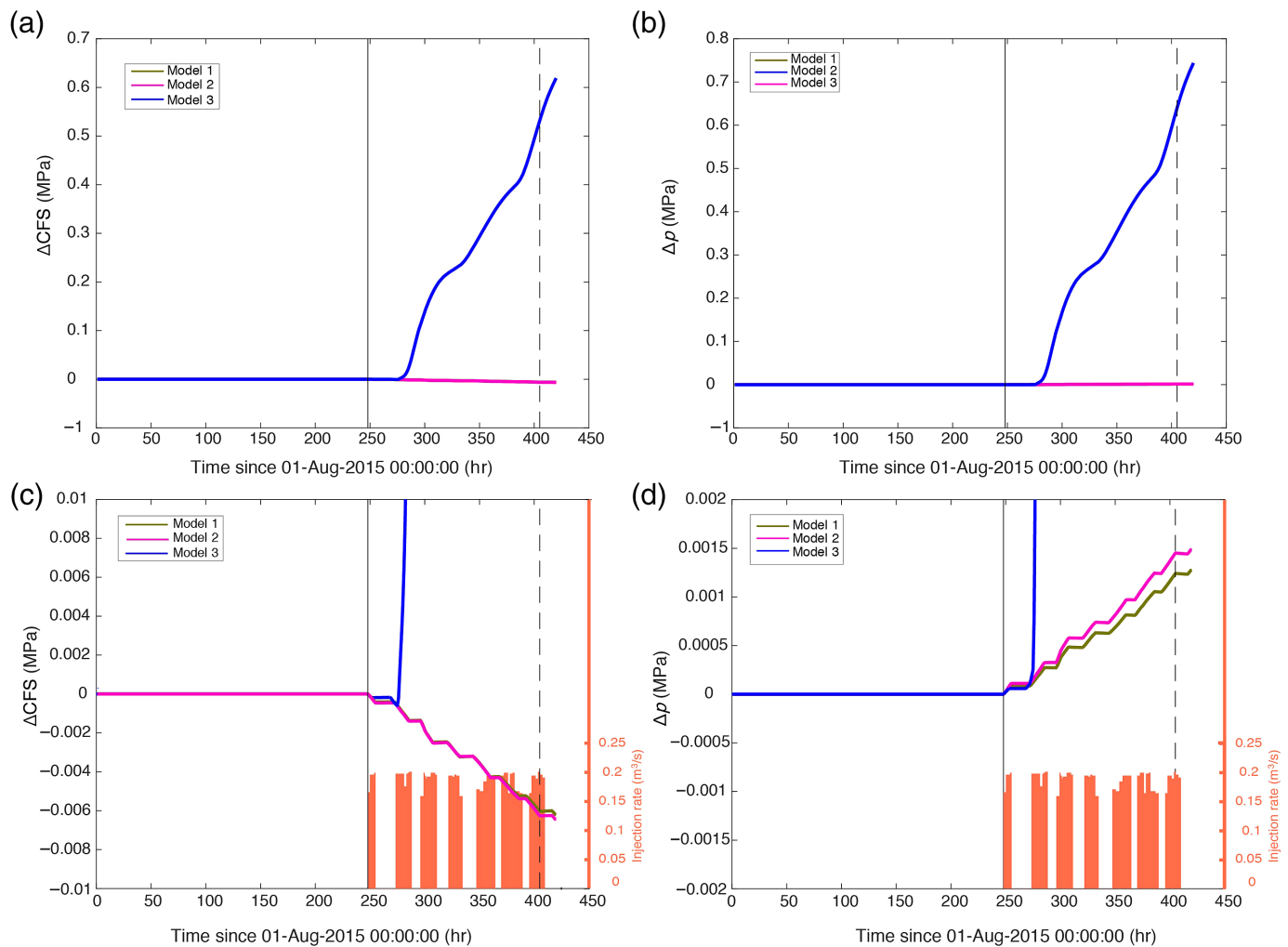
Poroelastic models for nearby HF sites (W2 and W3)

Next, we focus on the different seismogenic behavior at the two nearby HF sites (W2 and W3, Fig. 1). Here, we refer to the one-day seismic response as immediate triggering at W2 and W3, compared to the five-day response time at W1 (i.e., delayed triggering). The seismicity and detailed operational period for W1, W2, and W3 can be found in Figure S2. We follow the method used in the [Poroelastic models for the \$M_w\$ 4.6 mainshock](#) section, to calculate the ΔCFS imposed on the receiver faults, by coupling progression of the elastic stress and pore pressure changes from the injected fluids, and the details are as follows.

We simulate W2 and W3 separately, but the model setup is the same ($20 \text{ km} \times 20 \text{ km} \times 5 \text{ km}$, as shown in Fig. S3). The number of layers, solid and hydrogeological properties, and

Figure 3. The four-layer model built with COMSOL to simulate the triggering mechanisms of the M_w 4.6 earthquake. (a) The hydrostatic pore pressure from the transient model before HF starts, which is used as the initial value input for the following time-dependent study. (b) Model 1, the square in the fourth layer denotes the fault patch, and the dashed points represent the injection points for each stage. (c) Model 2, similar to model 1, but with a high-permeable fracture zone caused by HF operation, as indicated by the cube in the second shale layer. (d) Model 3, similar to model 2, but with a high-permeable conduit represented by the vertical cylinder. The properties for each layer and structure can be found in Table S1. The color version of this figure is available only in the electronic edition.

boundary and initial conditions are identical to the models described in the [Poroelastic models for the \$M_w\$ 4.6 mainshock](#) section. In both the cases, we choose the first earthquake in each sequence as the representative location of the receiver fault (named as E2 and E3 for injections at W2 and W3, respectively, Fig. S3), and simulate the cumulative effects from previous injections (i.e., effects from W1 on E2, and effects from both W1 and W2 on E3, given the injection timing as

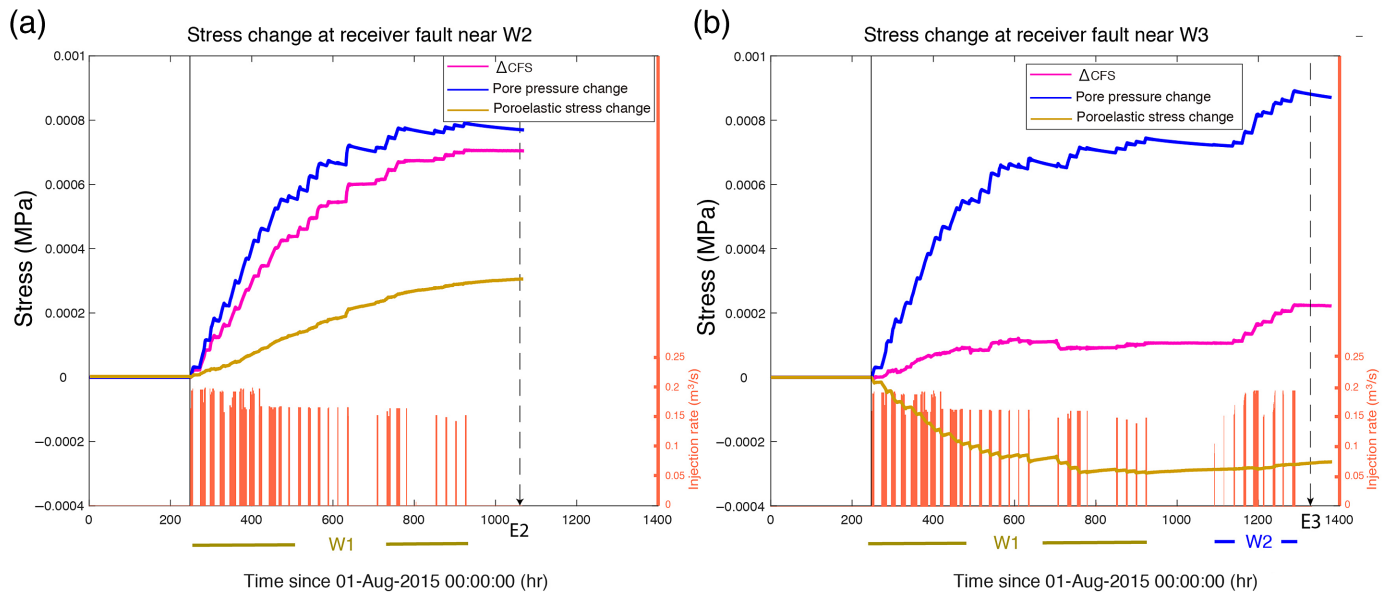


indicated in Fig. 5 and Fig. S2). Because no reliable fault-plane solutions exist for the two selected events, the two receiver faults are assumed to be optimally oriented with respect to the local tectonic stress field (e.g., Bell and Grasby, 2012), when calculating the corresponding ΔCFS (equation 8). Unlike the three scenarios used for W1 (Fig. 3b–d), we only simulate the simplest configuration without the existence of the fracture zone around the horizontal wells or hydrological conduits (i.e., similar to model 1), as the scale of the fracture zone or fault is much smaller than the distances between the injection sites. The results of the ΔCFS , pore pressure change, and poroelastic stress change are shown in Figure 5.

We point out several notable features of the temporal evolution of the ΔCFS and pore pressure calculated for E2 and E3 (Fig. 5). First, the ΔCFS shows a similar monotonic increase, when there is fluid injection operation, but, the amplitude is smaller at E3 (Fig. 5b), due to the negative poroelastic stress change. Second, it is clear that the ΔCFS results calculated with the poroelastic model on E2 and E3 both have positive values, suggesting that the nearby HF injections could facilitate the faulting process. However, previous studies report that the spatial distribution of aftershocks appears to correlate with regions

Figure 4. ΔCFS and pore pressure change (Δp) results for the poroelastic models 1, 2, and 3. (a,b) The results for the three models and (c,d) the enlarged version for models 1 and 2. (a,c) The ΔCFS calculated using equation (8). (b,d) Pore pressure changes only. The solid vertical lines represent the onset time of HF operations, and the dashed vertical lines represent the occurrence time of the M_w 4.6 earthquake. The bottom bars represent the fluid injection rate and duration for individual HF stages. The color version of this figure is available only in the electronic edition.

with $\Delta CFS \geq 0.01$ – 0.02 MPa (e.g., Harris and Simpson, 1992; Gross and Kisslinger, 1997; Stein, 1999). If we take the most conservative approach, by setting the static stress triggering threshold to be 0.02 MPa, we acknowledge that the simulated ΔCFS at the timing of E2 and E3 is, at least, one order of magnitude smaller. Third, there are simultaneous step-like jumps of the ΔCFS and pore pressure change in response to the HF operations. Finally, we note that the ΔCFS at E3 is smaller than that at E2, even though E3 is subject to effects from injections at both W1 and W2, whereas, E2 is affected only by injection W1. The difference can be explained by the relative positions of the three injection sites. As the orientation of the fault is an important factor controlling the amplitude of



Δ CFS (Eq. 8), the stress changes caused by injection at W1 and W2, to a large degree, cancel at E3. On the other hand, the pore pressure change exhibits similar behavior at E2 and E3, because it is less sensitive to the directional factor. Such cumulative effect (in either positive or negative sense) due to injection at multiple wells and well-to-fault relative location are also suggested to be controlling factors for the occurrences of earthquakes related to wastewater disposal in Oklahoma (Deng *et al.*, 2020).

DISCUSSION AND IMPLICATION

As shown in Figure 4, considering the Δ CFS from the three models, the M_w 4.6 earthquake is more likely to have been triggered by the elevated pore pressure associated with the migration of injected fluid through pathways of relatively high permeability, as suggested by model 3. Because Figure 4 only shows a fixed permeability of the conduit, we conduct additional tests to investigate how the Δ CFS on the receiver fault varies with the magnitude of permeability of the conduit in model 3. Modeling results in Figure S4 suggest that a minimum permeability of $\sim 1.5 \times 10^{-13} \text{ m}^2$ is required to accumulate enough pore pressure on the fault surface to reach the triggering threshold, as indicated with the black horizontal dashed line (i.e., 0.02 MPa, Stein, 1999). At last, we test a range of Biot coefficient (α) values, to investigate their influence on Δ CFS. The results suggest that the effect of different Biot coefficient values on Δ CFS is small (Fig. S5), and, therefore, is unlikely to alter our conclusions.

Although, the conduit in model 3 is an assumption, several factors may hint its potential existence. First, because the Δ CFS calculated on the receiver fault in both models 1 and 2 are negative, the existence of a conduit is probably a necessary condition to flip the sign of Δ CFS (Fig. 4). Second, previous studies suggested that the Dawson Creek Graben Complex hosts a

Figure 5. Stress change as a function of time for the receiver faults at injection sites near (a) W2 and (b) W3. The location of the receiver faults is shown in Figure S3. The bottom bars represent the fluid injection rate and duration for individual HF stages. The solid vertical lines represent the onset time of HF operations, and the dashed vertical lines represent the occurrence time of E2 and E3. The poroelastic stress change is calculated with Δ CFS = $\Delta\tau + \mu\Delta\sigma$, without considering the pore pressure change Δp . The color version of this figure is available only in the electronic edition.

number of faults in the Precambrian crystalline basement developed during the subsidence process (e.g., Berger, 1994). The extended fault system and the associated fracture zones can act as pathways of elevated permeability, connecting the reservoir and Precambrian crystalline basement (e.g., Kozłowska *et al.*, 2018). Third, the Leduc Reef structures and fault-related karst features may form the conduit for the fluid to migrate vertically in Alberta (Schultz *et al.*, 2016; Galloway *et al.*, 2018). We speculate that similar structures may also exist in British Columbia. The presence of a highly permeable fluid conduit is also proposed as the most likely triggering mechanism for the M_L 4.5 earthquake in the Kiskatinaw area, $\sim 140 \text{ km}$ from the M_w 4.5 in this study (Peña Castro *et al.*, 2020). It is worth noting that the geometry of the conduit in model 3 is simplified to be a cylinder, directly connecting the horizontal wells and the preexisting fault. To test the effect of the assumed conduit geometry, we conduct additional experiments by substituting the cylinder conduit with a planar conduit. The two shapes give similar results (Fig. S6), except that the planar conduit requires a slightly larger permeability ($\sim 1.8 \times 10^{-13} \text{ m}^2$) to reach the triggering threshold (Fig. S6). Finally, we point out that a more realistic combination of horizontal and dipping faults could also act as conduit-like structures to achieve the required Δ CFS.

Fault orientation represents an important factor in the determination of the ΔCFS required, to activate a fault (e.g., [Lei et al., 2017](#)). We investigate how different fault types and strike and dip angles could influence the amplitude of the ΔCFS on the receiver fault of the M_w 4.6 earthquake, by assuming that the required stress perturbation to reactivate this preexisting fault will be the same for all types and orientations of faults (i.e., 0.02 MPa) (details are available in the supplemental material). We find that if the fluid has migrated to the fault, then the pore pressure will be the dominant factor affecting the ΔCFS , regardless of the orientation of the fault (Fig. 6 for reverse fault, Figs. S7 and S8 for normal and strike-slip fault, respectively). Accordingly, [Cochran et al. \(2020\)](#) also suggest that the 2011 Prague, Oklahoma, wastewater-disposal-induced sequence occurred on both optimally and unfavorably oriented faults. Thus, the estimate depicted in Figure 6, Figures S7, and S8 supports the inference that direct pore pressure migration through permeable pathways is the most likely mechanism to achieve the >0.02 MPa stress perturbation on the M_w 4.6 fault.

Nonetheless, we do not rule out the possibility that very small ΔCFS (<0.002 MPa) from poroelastic stress transfer could trigger tectonic earthquakes. For example, if the preexisting fault system is already at a critically stressed state and optimally oriented, as suggested by other studies, stress perturbation from teleseismic events with only several kilopascals could be enough to trigger local earthquakes, when using dynamic triggering as a probe (e.g., [van der Elst et al., 2013](#); [Wang et al., 2015, 2018](#)). Given the lack of knowledge on the stress state of the fault, there is no easy way to unambiguously infer the elastic stress transfer as the dominant triggering mechanism for the M_w 4.6 earthquake. Instead, elevated pore pressure due to rapid fluid migration via conduit-like pathways (Fig. 3d) may provide the most straightforward scenario of what has occurred. The results here suggest that the sole implication of the traditional traffic light protocol (TLP) may not be enough to assess the potential seismic hazard induced by HF operations ([Kao et al., 2018](#)), because the TLP does not consider any potential preexisting faults or conduit-like pathways.

[Deng et al. \(2016\)](#) suggest that the elastic response of the solid matrix could be the dominant triggering factor for earthquakes induced by HF, instead of fluid pore pressure change. However, in our case, the sole elastic stress perturbations for models 1 and 2 are likely too small (and, at times, exhibit negative ΔCFS) to have triggered the M_w 4.6 mainshock. The relatively small elastic response can be explained in several ways. First of all, one of the most important factors controlling the amplitude of poroelastic stress is distance (e.g., [Segall and Lu, 2015](#)). [Deng et al. \(2016\)](#) calculate the ΔCFS on a reference point shallower and closer to the HF horizontal well (as shown in their fig. 2), whereas, in our case, the fault plane is farther and deeper from the HF injection point (~ 4 km depth).

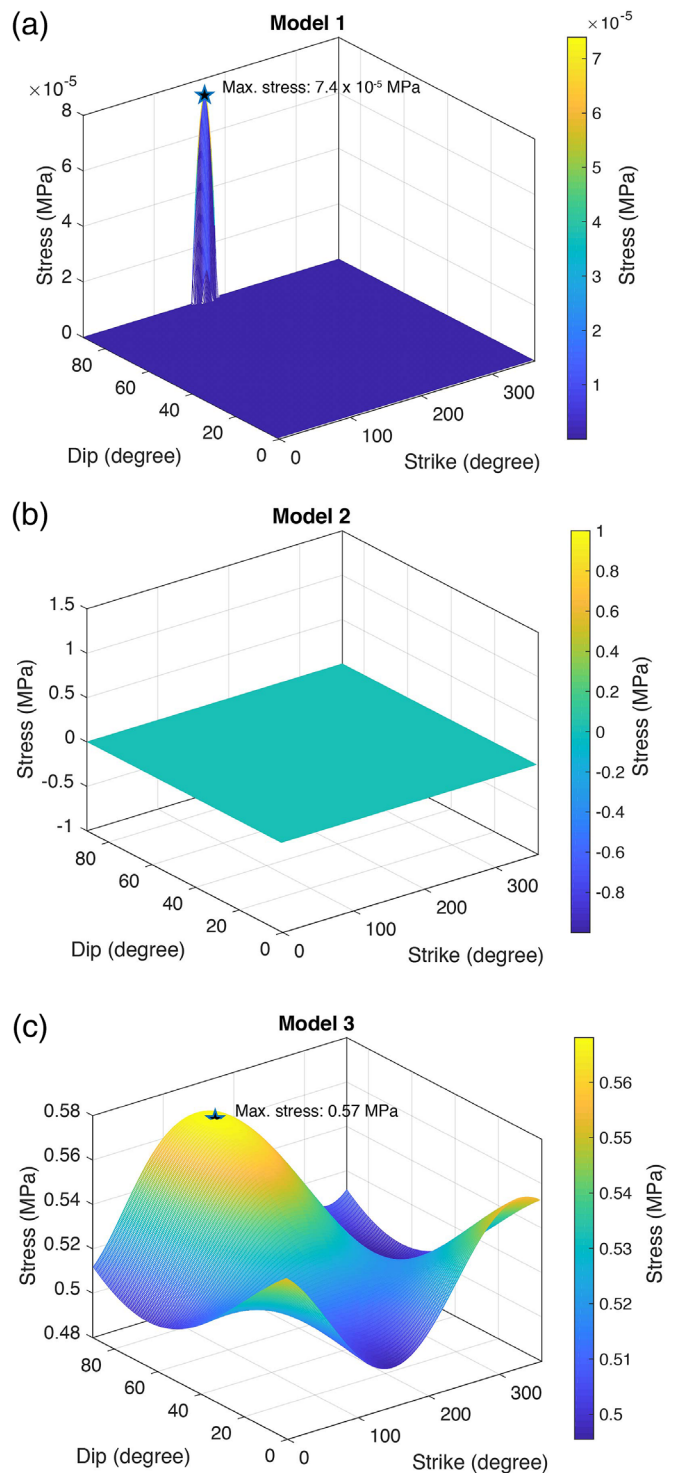


Figure 6. The maximum ΔCFS for a range of strike and dip combinations on the receiver fault (M_w 4.6 reverse faulting event). (a) The maximum ΔCFS calculated for model 1, for which only positive ΔCFS is shown here, and negative ΔCFS is shown as 0 values. (b,c) The maximum ΔCFS calculated for models 2 and 3, respectively. The color version of this figure is available only in the electronic edition.

Second, the injection volume per HF stage in our study is about one-half of the case presented in [Deng et al. \(2016\)](#) ($\sim 1300 \text{ m}^3$ vs. 2700 m^3), and the simulated shale layer in our study is ~ 5 – 6 times thicker than that in their case, in which both factors lead to less solid deformation. Third, we assume a higher permeability along the receiver fault surface, which is not used in the case of [Deng et al. \(2016\)](#). This assumption could potentially influence the pore pressure change on the fault surface. Another noticeable difference between our results and that of [Deng et al. \(2016\)](#) is the simultaneous step-like response of pore pressure change to the HF operations (Figs. 4 and 5). This discrepancy could be due to the scale of y axis used in their figures. Nevertheless, the transient response of solid deformation within the rock matrix to the pore pressure change at the injection points is not, particularly, surprising, as the two phenomena are fully coupled in poroelastic models. We note, however, that the elastic stress perturbation could act as the dominant triggering factor for injection-induced earthquakes only, when two conditions are met at the same time: (1) the delay times between the HF operation and induced seismicity are too short, and/or the distance between the injection well and the receiver fault is too long for the pore pressure increase to reach the fault, and (2) the receiver faults are in the positive quadrants of ΔCFS , with values exceeding the triggering threshold.

Studies suggest that fracture openings, as a response to HF operations, could also play a role on the distribution and triggering of induced earthquakes (e.g., [Bao and Eaton, 2016](#); [Kettlety et al., 2020](#)). To test whether the M_w 4.6 earthquake could be related to the elastic responses related to hydraulic (mode I) fracture openings, we also calculate the ΔCFS imposed by fractures opening during the stimulation of successive stages on the preexisting fault (see supplemental material). The results show that the maximum ΔCFS is $\sim 0.003 \text{ MPa}$ at the 3 km depth but quickly drops to $\sim 0.001 \text{ MPa}$ at 5 km (Fig. S9). As even the larger values at 3 km are significantly smaller than the static stress triggering threshold (0.02 MPa , e.g., [Reasenber and Simpson, 1992](#); [Stein, 1999](#)), we do not regard the fracture opening due to fluid injection as the dominant triggering mechanism.

Given that the ΔCFS at E2 and E3 are too small to reactivate a shear dislocation (Fig. 5), the almost instantaneous seismic response to nearby HF injection suggests that additional factors not included in our poroelastic models should also be considered. For example, although, our models do not include any conduit-like structures, we cannot rule out the possibility that a complex conduit system could exist on a broader scale and may facilitate the fluid pressure migration process. For example, a number of regional faults, such as the Bonanza fault and the Gordondale fault, have been documented across northeastern British Columbia and northwestern Alberta (e.g., [Mossop and Shetsen, 1994](#)). In addition, the M_w 4.6 mainshock may exert nonnegligible effects, in combination with fracture openings from nearby HF operations. To verify this hypothesis, we first

calculate the ΔCFS that is caused by the combined effects of the HF fractures opening at W1 and the M_w 4.6 mainshock at E2 (Fig. S10a–c). We then calculate the ΔCFS at E3 resulting from the combined effects of HF fracture openings at W1 and W2, as well as the M_w 4.6 mainshock (Fig. S10d–f). The small positive Coulomb stress increase suggests a very minor effect to help facilitate the quick seismic responses at E2 and E3. Finally, some other factors, such as the difference between the current level of stress on the faults and the required stress level of failure (i.e., how large a stress perturbation is required to activate faulting), the specific geological settings at W2 and W3, the spatial heterogeneity of the tectonic stress within such a small region ($\sim 10 \text{ km}$), could all influence the seismic response time. Without further details on local structures, their effects are difficult to assess and, therefore, will not be discussed here.

Despite using multiple numerical models, to simulate the effects of various hydrogeological scenarios, we acknowledge that the results of numerical simulations may suffer from the lack of detailed a priori information on many physical parameters, including the precise size of the fracture zones, the dimension and orientation of the local fault systems, the initial confining pressure in the shale layer, the 3D distribution of different geological layers, and the geometry and physical properties of the potential conduit systems. Taking the confining pressure into consideration, for example, the conventional wisdom is that overpressure in the sedimentary section could lead to a reduction of fault strength and an increase in the porosity and permeability (e.g., [Suppe, 2014](#)). Thus, the hydrostatic condition assumed in our models may underestimate the porosity and permeability of the formations, leading to a relatively smaller ΔCFS on the fault surface. Moreover, the stress transfer through aseismic slip to the fault surface could also contribute to the fault reactivation process (e.g., [Eyre et al., 2019](#); [Bhattacharya and Viesca, 2019](#)). Unfortunately, the nature of aseismic slip, if exists, can only be assessed through high-resolution geodetic observations that are unavailable in our study area. Without any information on the detailed spatiotemporal distribution of possible aseismic slip caused by HF, we cannot quantify the corresponding stress perturbation. With improved observations (e.g., high-resolution seismic images, in situ borehole logs, formation pressure measurements, and geodetic monitoring) and more comprehensive understanding of all of the variables and mechanisms, we expect to further increase the model accuracy and make the numerical simulations as close to realistic scenarios as possible.

CONCLUSIONS

We employ the Coulomb failure criteria to investigate the triggering mechanism of the largest (M_w 4.6) HF-induced earthquake sequence in Canada. We use poroelastic simulation to calculate the coupled evolution of elastic stress and pore pressure changes caused by HF fluid injections on the

corresponding receiver faults. For the M_w 4.6 mainshock, we compare three different scenarios: the first scenario simulates the spatiotemporal effect due to HF injection stages only, the second scenario adds a fracture zone around the HF horizontal wells, and the third scenario further adds a conduit to connect the HF well and the receiver fault.

Our results suggest that a conduit-like structure can efficiently facilitate the migration of fluid from the injection well (W1) to the receiver fault and destabilize the fault, thus, best explains the observed five-day delay since the start of HF injection. The sole elastic stress perturbation ($\Delta CFS \sim -0.005$ MPa) caused by interactions between the injected fluids and rock matrix is too small (and negative) to trigger the fault slip, even with full consideration of the fault orientation effect. It is worth noting that due to lack of geodetic data, we cannot estimate the stress transfer from aseismic slip, thus we make no further inferences here.

We investigate the immediate seismic response at the two nearby HF sites (W2 and W3), by conducting the same analysis, to examine the cumulative effects from all HF stimulations. The results suggest that the poroelastic stress perturbation, the M_w 4.6 mainshock, and the fracture openings could work collectively to alter the local stress field and, thus, contribute to the immediate seismic response.

Our results have important implications for the energy industry and regulators, to establish effective strategies focusing on the mitigation of seismic hazard from induced earthquakes. A detailed mapping of the location and geometry of preexisting faults in the HF operation area is necessary and should be required to provide the first-order evaluation of induced seismic risk. Finally, structures with high permeability can be effective conduits for fluid migration and should be avoided at all stages of HF operations.

DATA AND RESOURCES

Earthquake catalog is adopted from Wang *et al.* (2020). Seismic waveforms for Natural Resources Canada (NRCAN) stations are publicly available at the Incorporated Research Institutions for Seismology (IRIS) (network code CN). Waveform data from MG stations used in this study will be available following a temporary embargo, and users who require immediate access may send requests to R. M. Harrington. Hydraulic fracturing (HF) injection data are available at the B.C. Oil and Gas Commission's online database at <https://www.bcogc.ca/data-reports/data-centre/> (last accessed May 2020). The supplemental material to this article includes a supplemental text document (detailing ΔCFS calculation caused by fracture opening), eight figures (velocity model, fluid injection rate, and the location of earthquakes used for immediate seismic response, ΔCFS results with different permeability of the conduit, the maximum ΔCFS for a range of strike and dip combinations on the normal and strike slip faulting, and ΔCFS calculated with fracture openings). In addition, one table listing the solid and fluid properties used in the three numerical models is provided.

ACKNOWLEDGMENTS

The authors thank Jeremy Maurer and Dmitry Garagash for their construction reviews, the Canadian Hazard Information Service and the Induced Seismicity Research Project, Environmental Geoscience Program of Natural Resources Canada (NRCAN) for routine maintenance of stations in northeast British Columbia, Incorporated Research Institutions for Seismology Data Management Center (IRIS-DMC) for providing data service, Conan Drummond for help with station installation, and Mark Norton for obtaining station permit. This study is funded by a Geoscience BC grant (HK), Natural Science and Engineering Research Council Discovery grants (RMH, YL, and HK), and startup funds from the Ruhr University Bochum (RMH). NRCAN Contribution Number 20200588.

REFERENCES

- Aki, K., and P. G. Richards (2002). *Quantitative Seismology*, University Science Books, Herndon, Virginia, 704 pp.
- Atkinson, G. M., D. W. Eaton, H. Ghofrani, D. Walker, B. Cheadle, R. Schultz, R. Shcherbakov, K. Tiampo, J. Gu, R. M. Harrington, *et al.* (2016). Hydraulic fracturing and seismicity in the Western Canada sedimentary basin, *Seismol. Res. Lett.* **87**, 631–647.
- Azad, M., D. Garagash, and M. Satish (2017). Nucleation of dynamic slip on a hydraulically fractured fault, *J. Geophys. Res.* **122**, 2812–2830.
- Bao, X., and D. W. Eaton (2016). Fault activation by hydraulic fracturing in western Canada, *Science* **354**, 1406–1409.
- B.C. Oil and Gas Commission (2012). Investigation of observed seismicity in the Horn River basin, *Technical Rept.*, available at <https://www.bcogc.ca/files/reports/Technical-Reports/investigation20of20observed20seismicity20in20the20horn20river20basinaug202012.pdf> (last accessed December 2020).
- Bell, J., and S. Grasby (2012). The stress regime of the Western Canadian sedimentary basin, *Geofluids* **12**, 150–165.
- Berger, Z. (Editor) (1994). The Fort St. John Graben, Western Canada, in *Satellite Hydrocarbon Exploration*, Springer, Berlin-Heidelberg, 239–248, doi: [10.1007/978-3-642-78587-0_13](https://doi.org/10.1007/978-3-642-78587-0_13).
- Bhattacharya, P., and R. C. Viesca (2019). Fluid-Induced aseismic fault slip outpaces pore-fluid migration, *Science* **364**, 464–468.
- Cappa, F. (2009). Modelling fluid transfer and slip in a fault zone when integrating heterogeneous hydromechanical characteristics in its internal structure, *Geophys. J. Int.* **178**, 1357–1362.
- Clauser, C. (1992). Permeability of crystalline rocks, *Eos Trans. AGU* **73**, 233–238.
- Cochran, E. S., R. J. Skoumal, D. McPhillips, Z. E. Ross, and K. M. Keranen (2020). Activation of optimally and unfavourably oriented faults in a uniform local stress field during the 2011 Prague, Oklahoma, sequence, *Geophys. J. Int.* **222**, 153–168.
- Cui, X., and B. Nassichuk (2018). Permeability of the Montney Formation in the Western Canada sedimentary basin: Insights from different laboratory measurements, *Bull. Can. Petrol. Geol.* **66**, 394–424.
- Davies, G. R., T. F. Moslow, and M. D. Sherwin (1997). The lower triassic Montney Formation, west-central Alberta, *Bull. Can. Petrol. Geol.* **45**, 474–505.
- Deng, K., Y. Liu, and X. Chen (2020). Correlation between poroelastic stress perturbation and multidisposal wells induced earthquake

- sequence in Cushing, Oklahoma, *Geophys. Res. Lett.* **47**, e2020GL089366, doi: [10.1029/2020GL089366](https://doi.org/10.1029/2020GL089366).
- Deng, K., Y. Liu, and R. M. Harrington (2016). Poroelastic stress triggering of the December 2013 Crooked Lake, Alberta, induced seismicity sequence, *Geophys. Res. Lett.* **43**, 8482–8491.
- Detournay, E., and A. H.-D. Cheng (1993). Fundamentals of poroelasticity, in *Analysis and Design Methods*, C. Fairhurst (Editor), Elsevier, Amsterdam, The Netherlands, 113–171.
- Dong, T., N. B. Harris, K. Ayranci, C. E. Twemlow, and B. R. Nassichuk (2017). The impact of composition on pore throat size and permeability in high maturity shales: Middle and Upper Devonian Horn River Group, northeastern British Columbia, Canada, *Mar. Petrol. Geol.* **81**, 220–236.
- Ellsworth, W. L. (2013). Injection-induced earthquakes, *Science* **341**, 1225942.
- Eyre, T. S., D. W. Eaton, D. I. Garagash, M. Zecevic, M. Venieri, R. Weir, and D. C. Lawton (2019). The role of aseismic slip in hydraulic fracturing-induced seismicity, *Sci. Adv.* **5**, eaav7172, doi: [10.1126/sciadv.aav7172](https://doi.org/10.1126/sciadv.aav7172).
- Farrell, N., D. Healy, and C. Taylor (2014). Anisotropy of permeability in faulted porous sandstones, *J. Struct. Geol.* **63**, 50–67.
- Galis, M., J. P. Ampuero, P. M. Mai, and F. Cappa (2017). Induced seismicity provides insight into why earthquake ruptures stop, *Sci. Adv.* **3**, eaap7528, doi: [10.1126/sciadv.aap7528](https://doi.org/10.1126/sciadv.aap7528).
- Galloway, E., T. Hauck, H. Corlett, D. Panã, and R. Schultz (2018). Faults and associated karst collapse suggest conduits for fluid flow that influence hydraulic fracturing-induced seismicity, *Proc. Natl. Acad. Sci.* **115**, E10003–E10012.
- Garagash, D. I., and L. N. Germanovich (2012). Nucleation and arrest of dynamic slip on a pressurized fault, *J. Geophys. Res.* **117**, no. B10, doi: [10.1029/2012JB009209](https://doi.org/10.1029/2012JB009209).
- Goebel, T., M. Weingarten, X. Chen, J. Haffener, and E. Brodsky (2017). The 2016 Mw5.1 Fairview, Oklahoma earthquakes: Evidence for long-range poroelastic triggering at >40 km from fluid disposal wells, *Earth Planet. Sci. Lett.* **472**, 50–61.
- Gross, S., and C. Kisslinger (1997). Estimating tectonic stress rate and state with Landers aftershocks, *J. Geophys. Res.* **102**, 7603–7612.
- Guglielmi, Y., F. Cappa, J.-P. Avouac, P. Henry, and D. Elsworth (2015). Seismicity triggered by fluid injection-induced aseismic slip, *Science* **348**, 1224–1226.
- Harris, R. A. (1998). Introduction to special section: Stress triggers, stress shadows, and implications for seismic hazard, *J. Geophys. Res.* **103**, 24,347–24,358.
- Harris, R. A., and R. W. Simpson (1992). Changes in static stress on southern California faults after the 1992 Landers earthquake, *Nature* **360**, 251–254.
- Healy, J. H., W. W. Rubey, D. T. Griggs, and C. B. Raleigh (1968). The Denver earthquakes, *Science* **161**, 1301–1310.
- Hsieh, P. A., and J. D. Bredehoeft (1981). A reservoir analysis of the Denver earthquakes: A case of induced seismicity, *J. Geophys. Res.* **86**, 903–920.
- Kao, H., S.-J. Shan, A. Bent, C. Woodgold, G. Rogers, J. F. Cassidy, and J. Ristau (2012). Regional centroid-moment-tensor analysis for earthquakes in Canada and adjacent regions: An update, *Seismol. Res. Lett.* **83**, 505–515.
- Kao, H., R. Visser, B. Smith, and S. Venables (2018). Performance assessment of the induced seismicity traffic light protocol for northeastern British Columbia and western Alberta, *The Leading Edge* **37**, 117–126.
- Keranen, K., M. Weingarten, G. Abers, B. Bekins, and S. Ge (2014). Sharp increase in central Oklahoma seismicity since 2008 induced by massive wastewater injection, *Science* **345**, 448–451.
- Kettlety, T., J. Verdon, M. Werner, and J. Kendall (2020). Stress transfer from opening hydraulic fractures controls the distribution of induced seismicity, *J. Geophys. Res.* **125**, e2019JB018794, doi: [10.1029/2019JB018794](https://doi.org/10.1029/2019JB018794).
- Kim, W.-Y. (2013). Induced seismicity associated with fluid injection into a deep well in Youngstown, Ohio, *J. Geophys. Res.* **118**, 3506–3518.
- Kozłowska, M., M. R. Brudzinski, P. Friberg, R. J. Skoumal, N. D. Baxter, and B. S. Currie (2018). Maturity of nearby faults influences seismic hazard from hydraulic fracturing, *Proc. Natl. Acad. Sci. Unit. States Am.* **115**, E1720–E1729.
- Laske, G., G. Masters, Z. Ma, and M. Pasyanos (2013). Update on CRUST1.0—A 1-degree global model of Earth's crust, *Geophysical Research Abstracts, EGU General Assembly*, Vienna, Austria, 2658 pp.
- Leake, S., and P. A. Hsieh (1995). Simulation of deformation of sediments from decline of ground-water levels in an aquifer underlain by a bedrock step, *U.S. Geol. Surv. Subsidence Interest Group Conference, Proc. of the Technical Meeting*, Las Vegas, Nevada, 14–16 February 1995, 10 pp.
- Lei, X., D. Huang, J. Su, G. Jiang, X. Wang, H. Wang, X. Guo, and H. Fu (2017). Fault reactivation and earthquakes with magnitudes of up to Mw 4.7 induced by shale-gas hydraulic fracturing in Sichuan Basin, China, *Sci. Rep.* **7**, no. 7971, 1–12.
- Lin, J., and R. S. Stein (2004). Stress triggering in thrust and subduction earthquakes and stress interaction between the southern San Andreas and nearby thrust and strike-slip faults, *J. Geophys. Res.* **109**, no. B2, doi: [10.1029/2003JB002607](https://doi.org/10.1029/2003JB002607).
- Madariaga, R. (1977). Implications of stress-drop models of earthquakes for the inversion of stress drop from seismic observations, in *Stress in the Earth*, M. Wyss (Editor), Springer, Basel, Switzerland, 301–316.
- Mahani, A. B., R. Schultz, H. Kao, D. Walker, J. Johnson, and C. Salas (2017). Fluid injection and seismic activity in the northern Montney play, British Columbia, Canada, with special reference to the 17 August 2015 Mw 4.6 induced earthquake, *Bull. Seismol. Soc. Am.* **107**, 542–552.
- Maurer, J., E. M. Dunham, and P. Segall (2020). Role of fluid injection on earthquake size in dynamic rupture simulations on rough faults, *Geophys. Res. Lett.* **47**, e2020GL088377, doi: [10.1029/2020GL088377](https://doi.org/10.1029/2020GL088377).
- Mossop, G. D., and I. Shetsen (1994). *Geological Atlas of the Western Canada Sedimentary Basin*, Canadian Society of Petroleum Geologists, available at <https://www.ags.aer.ca/reports/atlas-of-the-western-canada-sedimentary-basin.html> (last accessed May 2020).
- Neuzil, C. (1994). How permeable are clays and shales?, *Water Resour. Res.* **30**, 145–150.
- Peña Castro, A. F., M. P. Roth, A. Verdecchia, J. Onwumeka, Y. Liu, R. M. Harrington, Y. Zhang, and H. Kao (2020). Stress chatter via fluid flow and fault slip in a hydraulic fracturing-induced

- earthquake sequence in the Montney Formation, British Columbia, *Geophys. Res. Lett.* **47**, e2020GL087254, doi: [10.1029/2020GL087254](https://doi.org/10.1029/2020GL087254).
- Reasenber, P. A., and R. W. Simpson (1992). Response of regional seismicity to the static stress change produced by the Loma Prieta earthquake, *Science* **255**, 1687–1690.
- Rice, J. R., and M. P. Cleary (1976). Some basic stress diffusion solutions for fluid-saturated elastic porous media with compressible constituents, *Rev. Geophys.* **14**, 227–241.
- Rokosh, C., J. Pawlowicz, H. Berhane, S. Anderson, and A. Beaton (2008). Geochemical and sedimentological investigation of Banff and Exshaw formations for Shale Gas potential; initial results, *Energ. Resour. Conservat. Board, ERCB/AGS Open-File Rept. 10*, 46 pp.
- Rokosh, C. D., S. D. Anderson, A. P. Beaton, M. Berhane, and J. Pawlowicz (2010). Geochemical and geological characterization of the Duvernay and Muskwa Formation in Alberta, *Canadian Unconventional Resources and International Petroleum Conference*, Society of Petroleum Engineers, doi: [10.2118/137799-MS](https://doi.org/10.2118/137799-MS).
- Roth, M. P., A. Verdecchia, R. M. Harrington, and Y. Liu (2020). High-resolution imaging of hydraulic-fracturing-induced earthquake clusters in the Dawson–Septimus area, Northeast British Columbia, Canada, *Seismol. Res. Lett.* **91**, no. 5, 2744–2756.
- Schultz, R., G. Atkinson, D. Eaton, Y. Gu, and H. Kao (2018). Hydraulic fracturing volume is associated with induced earthquake productivity in the Duvernay play, *Science* **359**, 304–308.
- Schultz, R., H. Corlett, K. Haug, K. Kocon, K. MacCormack, V. Stern, and T. Shipman (2016). Linking fossil reefs with earthquakes: Geologic insight to where induced seismicity occurs in Alberta, *Geophys. Res. Lett.* **43**, 2534–2542.
- Segall, P., and S. Lu (2015). Injection-induced seismicity: Poroelastic and earthquake nucleation effects, *J. Geophys. Res.* **120**, 5082–5103.
- Shapiro, S., and C. Dinske (2009). Fluid-induced seismicity: Pressure diffusion and hydraulic fracturing, *Geophys. Prospect.* **57**, 301–310.
- Stacy, S., J. Gomberg, and M. Cocco (2005). Introduction to special section: Stress transfer, earthquake triggering, and time-dependent seismic hazard, *J. Geophys. Res.* **110**, no. B5, doi: [10.1029/2005JB003692](https://doi.org/10.1029/2005JB003692).
- Stein, R. S. (1999). The role of stress transfer in earthquake occurrence, *Nature* **402**, 605.
- Suppe, J. (2014). Fluid overpressures and strength of the sedimentary upper crust, *J. Struct. Geol.* **69**, 481–492.
- van der Elst, N. J., H. M. Savage, K. M. Keranen, and G. A. Abers (2013). Enhanced remote earthquake triggering at fluid-injection sites in the Midwestern United States, *Science* **341**, 164–167.
- Vishkai, M., J. Wang, R. C. Wong, C. R. Clarkson, and I. D. Gates (2017). Modeling geomechanical properties in the Montney Formation, Alberta, Canada, *Int. J. Rock Mech. Min. Sci.* **96**, 94–105.
- Wang, B., R. M. Harrington, Y. Liu, H. Kao, and H. Yu (2018). Remote dynamic triggering of earthquakes in three unconventional Canadian hydrocarbon regions based on a multiple-station matched-filter approach, *Bull. Seismol. Soc. Am.* **109**, 372–386.
- Wang, B., R. M. Harrington, Y. Liu, H. Kao, and H. Yu (2020). A study on the largest hydraulic-fracturing-induced earthquake in Canada: Observations and static stress-drop estimation, *Bull. Seismol. Soc. Am.* **110**, 2283–2294.
- Wang, B., R. M. Harrington, Y. Liu, H. Yu, A. Carey, and N. J. Elst (2015). Isolated cases of remote dynamic triggering in Canada detected using cataloged earthquakes combined with a matched-filter approach, *Geophys. Res. Lett.* **42**, 5187–5196.
- Wang, R., and H.-J. Kumpel (2003). Poroelasticity: Efficient modeling of strongly coupled, slow deformation processes in a multilayered half-space, *Geophysics* **68**, 705–717.
- Weingarten, M., S. Ge, J. W. Godt, B. A. Bekins, and J. L. Rubinstein (2015). High-rate injection is associated with the increase in US mid-continent seismicity, *Science* **348**, 1336–1340.
- Xu, C., J. Wang, Z. Li, and J. Drummond (2010). Applying the Coulomb failure function with an optimally oriented plane to the 2008 Mw 7.9 Wenchuan earthquake triggering, *Tectonophysics* **491**, 119–126.
- Yehya, A., Z. Yang, and J. R. Rice (2018). Effect of fault architecture and permeability evolution on response to fluid injection, *J. Geophys. Res.* **123**, 9982–9997.
- Yu, H., R. M. Harrington, H. Kao, Y. Liu, R. E. Abercrombie, and B. Wang (2020). Well proximity governing stress drop variation and seismic attenuation associated with hydraulic fracturing induced earthquakes, *J. Geophys. Res.* **125**, e2020JB020103, doi: [10.1029/2020JB020103](https://doi.org/10.1029/2020JB020103).
- Yu, H., R. M. Harrington, Y. Liu, and B. Wang (2019). Induced seismicity driven by fluid diffusion revealed by a near-field hydraulic stimulation monitoring array in the Montney basin, British Columbia, *J. Geophys. Res.* **124**, 4694–4709.
- Yu, H., Y. Liu, R. M. Harrington, and M. Lamontagne (2016). Seismicity along St. Lawrence Paleorift faults overprinted by a meteorite impact structure in Charlevoix, Québec, Eastern Canada, *Bull. Seismol. Soc. Am.* **106**, 2663–2673.
- Yu, H., L. Zhao, Y. Liu, J. Ning, Q.-F. Chen, and J. Lin (2016). Stress adjustment revealed by seismicity and earthquake focal mechanisms in northeast China before and after the 2011 Tohoku-Oki earthquake, *Tectonophysics* **666**, 23–32.
- Zhu, L., and D. V. Helmberger (1996). Advancement in source estimation techniques using broadband regional seismograms, *Bull. Seismol. Soc. Am.* **86**, 1634–1641.
- Zhu, L., and L. A. Rivera (2002). A note on the dynamic and static displacements from a point source in multilayered media, *Geophys. J. Int.* **148**, 619–627.

Manuscript received 29 July 2020
Published online 23 February 2021